Springer

Acta Mechanica Sinica

CrossMark click for updates

• RESEARCH PAPER •

Acta Mech. Sin., Vol. 41, 124203 (2025)
https://doi.org/10.1007/s10409-024-24203-x

Static bending and wave propagation analyses of a flexoelectric semiconductor nanobeam incorporating antisymmetric thickness-stretch

Ziwen Guo, Gongye Zhang*, and Changwen Mi*

Jiangsu Key Laboratory of Mechanical Analysis for Infrastructure and Advanced Equipment, School of Civil Engineering, Southeast University, Nanjing 210096, China

Received June 25, 2024; accepted October 9, 2024; published online August 25, 2025

We examine the electromechanical field and charge redistribution within a flexoelectric semiconductor (FS) nanobeam, accounting for bending, fundamental thickness-shear, and antisymmetric thickness-stretch deformations. The coupled governing equations include microstructure, flexoelectric, and semiconductor effects, highlighting the interplay between mechanical displacement, electric potential, and charge carriers. For applications in flexoelectronic devices, the static bending of a simply supported FS beam induced by uniform pressure and wave propagation in an unbounded FS beam are analytically addressed using the derived framework. The effects of antisymmetric thickness-stretch on mechanical displacements and electron concentration perturbation, as well as size dependence of microstructure and flexoelectric effects, are identified. An interesting finding reveals that wave frequencies of the antisymmetric thickness-stretch mode, as anticipated by the proposed model, are larger compared to those of the model neglecting flexoelectric and semiconductor effects. For the first time, the cutoff frequency of antisymmetric thickness-stretch impacted by the two features is explained mathematically. These findings are beneficial for enhancing the performance of flexoelectronic sensors and electroacoustic devices.

Flexoelectric semiconductor, Size-dependent effect, Antisymmetric thickness-stretch, Principle of virtual work

Citation: Z. Guo, G. Zhang, and C. Mi, Static bending and wave propagation analyses of a flexoelectric semiconductor nanobeam incorporating antisymmetric thickness-stretch, Acta Mech. Sin. 41, 124203 (2025), https://doi.org/10.1007/s10409-024-24203-x

1. Introduction

Flexoelectricity, characterized by polarization due to non-uniform strain, is allowed by symmetry in all crystalline solids, rendering it a more widespread property compared to the traditional piezoelectric effect [1-10]. However, the polarization charge generated by flexoelectricity in bulk materials typically remains small, which limits its practical application. Interestingly, as strain gradients tend to increase inversely with diminishing sample size, the flexoelectric effect demonstrates a size-dependent behavior [11-17]. This feature presents a promising avenue for maximizing flexoelectric response by working at the nanoscale. As a result, flexoelectricity has garnered attention for its prospective utility in considerable applications such as nanogenerators, sensors, and actuators [3,18-21]. Notably, unlike their macroscopic counterparts, nanoscale structures exhibit a dependence on their characteristic sizes, known as the microstructure effect [22-24]. Hence, it is imperative to concurrently consider the size-dependent effects of flexoelectricity and microstructure while modeling flexoelectric devices.

Due to the absence of charge carriers, piezoelectric/flexoelectric dielectrics are limited to transmitting the function of an external electric field solely through induction. The advent of third-generation semiconductors in the last century has opened up a new possibility for integrating piezoelectric and semiconductor properties, with the goal of establishing a direct interrelation between mechanical motion and electronic devices [25,26]. Theoretical and experimental studies focus-

*Corresponding authors. E-mail addresses: gyzhang@seu.edu.cn (Gongye Zhang); mi@seu.edu.cn (Changwen Mi)
Executive Editor: Zishun Liu

ing on electronic behaviors at the interface/junction have formed a new field termed "piezotronics" [27-38]. Recently, Wang et al. [39] also demonstrated an interaction within centrosymmetric semiconductors between mechanical fields and mobile charges. This finding prompts systematic investigations into flexoelectronics. Sun et al. [40] conducted an empirical investigation into the current-voltage characteristics of a silicon-based Schottky barrier diode under various tip forces and clarified the tuning mechanism of flexoelectricity on charge motion behaviors. In pursuit of direct electromechanical functionality, Guo et al. [41] introduced the application of silicon flexoelectronic transistors. Their findings underscored that flexoelectric polarization induced in inhomogeneously strained crystals significantly affects the redistribution of charge carriers.

To elucidate the complex process by which mechanical force modulates free-carrier motions within flexoelectric semiconductors (FSs), mechanics researchers have conducted insightful investigations on FS fibers and films. Zhao et al. [42] employed the drift-diffusion theory to investigate the extension coupling electromechanical properties of a GaN nanowire, exploring the synergistic impacts arising from strain gradient-induced flexoelectricity. PN heterojunctions in an FS composite beam were numerically studied by Li et al. [43]. Qu et al. [44,45] established electromechanical coupling models of FS beams and their composite structures based on the Bernoulli-Euler theory. Moreover, Qu et al. [46] examined the interplay of acoustic waves and charge carriers in FS plates, employing diverse structural theories including Kirchhoff-Love and Mindlin-Reissner models. Taking into account the Mindlin-Medick assumption, Zhang et al. [47] realized charge redistribution through the warping of an FS composite beam.

The Mindlin-Medick assumption incorporates five deformation modes, which can be decoupled into two groups within uniform beams or plates. The first group consists of traditional extension, fundamental thickness-stretch, and (second-order) symmetric shear, while the other includes bending and fundamental thickness-shear [22]. The latter can actually be considered as a first-order truncation, wherein a higher-order deformation along the thickness direction (specifically, the antisymmetric thickness-stretch) remains unexplored. To better understand the role of antisymmetric thickness-stretch in regulating flexoelectronic performances and reveal potential new phenomena, this paper presents a main contribution to exploring the static bending and wave propagation properties of an FS nanobeam within antisymmetric thickness-stretch, where microstructure, flexoelectric, and semiconductor effects are fully investigated. The comprehension of these issues will contribute to a more accurate analysis of FS structures, thereby facilitating the optimization of flexoelectronic sensor and electroacoustic device designs.

The following outlines the structure of this paper: In Sect. 2, the governing equations and boundary conditions (BCs) for an FS nanobeam are rigorously deduced using the principle of virtual work (PVW). Section 3 presents numerical analyses focusing on two aspects—one is the static bending of a simply supported FS beam induced by a uniform pressure, and the other is the wave propagation in an unbounded FS beam. The paper concludes with summaries and key findings in Sect. 4.

2. One-dimensional governing equations of an FS beam

For *n*-type centrosymmetric semiconductors, the general constitutive relations describing strain gradient, flexoelectric, and semiconductor effects are as follows [25,45,48,49]:

$$T_{ij} = c_{ijkl} S_{kl}, \tag{1a}$$

$$\tau_{ijk} = g_{ijklmn}\eta_{lmn} - f_{lijk}E_l, \tag{1b}$$

$$D_i = \varepsilon_{ij}E_j + f_{ijkl}\eta_{jkl}, \tag{1c}$$

$$J_i^n = qn\mu_{ij}^n E_j + qD_{ij}^n N_j, \tag{1d}$$

where T_{ij} and τ_{ijk} are the Cauchy stress and higher-order stress tensors, respectively; D_i and J_i^n represent the electric displacement vector and electron current density vector; c_{ijkl}, f_{ijkl}, ε_{ij}, and g_{ijklmn} are the elastic constants, flexoelectric coefficients, dielectric constants, and higher-order elastic constants, respectively; the elementary charge, denoted as q, equals 1.6×10^{-19} C; n signifies the concentration of electrons; μ_{ij}^n and D_{ij}^n are the carrier mobility and diffusion constant for electrons; S_{kl} and η_{jkl} are defined as the strain and strain gradient components, respectively; E_j denotes the electric field, whereas N_j refers to the gradient of concentration of electrons. These quantities can be characterized by the following kinematic relations:

$$\begin{aligned} S_{ij} &= (u_{i,j} + u_{j,i})/2, \\ \eta_{ijk} &= S_{ij,k}, \\ E_i &= -\varphi_{,i}, \\ N_i &= n_{,i}, \end{aligned} \tag{2}$$

with u_i and φ standing for the mechanical displacement and electrostatic potential, respectively.

We treat $n = n_0 + \Delta n$, $n_0 = N_D^+$, where n_0 is the doping level for electrons; in contrast, Δn and N_D^+ are the concentration perturbation of electrons and concentration of ionized donors, respectively. For tiny concentration perturbations, Eq. (1d) may be linearized as

$$J_i^n \cong qn_0\mu_{ij}^n E_j + qD_{ij}^n N_j, \tag{3}$$

which is sufficient to describe the material behaviors.

Consider an FS beam featuring a rectangular cross-section, as illustrated in Fig. 1(a). Deformations of bending, fundamental thickness-shear, and thickness-stretch are considered and shown in Fig. 1(b)-(d). Following that, the displacement field in the FS beam can be described as

$$\begin{aligned}\mathbf{u}(\mathbf{x},t) &= u_i(\mathbf{x},t)\mathbf{e}_i \\ &= \left[x_3 u_1^{(1)}(x_1,t)\right]\mathbf{e}_1 + \left[u_3^{(0)}(x_1,t) + x_3^2 u_3^{(2)}(x_1,t)\right]\mathbf{e}_3,\end{aligned} \tag{4}$$

where $u_3^{(0)}$ and $u_1^{(1)}$ are the bending and fundamental thickness-shear, respectively; $u_3^{(2)}$ represents the (second-order) thickness-stretch. Note that $u_3^{(2)}$ discussed here is antisymmetric (Fig. 1(d)), which is different from the symmetric thickness-stretch that coupled with extension and symmetric shear [50].

The electric potential and electron concentration perturbation can be estimated using

$$\begin{aligned}\varphi(\mathbf{x},t) &\cong x_3\varphi^{(1)}(x_1,t), \\ \Delta n(\mathbf{x},t) &\cong x_3 n^{(1)}(x_1,t),\end{aligned} \tag{5}$$

where $\varphi^{(1)}$ and $n^{(1)}$ represent the first-order electric potential and first-order electron concentration, respectively. It is seen that Eq. (5) is limited to describing the variation of electric potential and electron concentration anti-symmetrically along the thickness direction of the beam. Note that a higher-order description is required for more complex distributions of φ and Δn [51]. Subsequently, the substitution of Eqs. (4) and (5) into Eq. (2) leads to the component forms of strain, strain gradient, electric field intensity, and electron concentration gradient in the FS beam.

Based on the PVW approach, the field equations and corresponding BCs of an arbitrary FS structure can be obtained from [52]

$$\delta W_{(d)} + \delta W_{(c)} + \delta W_{(i)} = 0, \tag{6}$$

where $\delta W_{(d)}$, $\delta W_{(c)}$, and $\delta W_{(i)}$ are defined as the virtual work of actions at a distance, contact forces, and internal forces [50]. In this circumstance, no surface phenomena are applied to the beam, i.e., $\delta W_{(c)} = 0$. $\delta W_{(d)}$ and $\delta W_{(i)}$ are

$$\delta W_{(d)} = -\int_V \left[(f_i - \rho\ddot{u}_i)\delta u_i - q(-n + N_D^+)\delta\varphi - \lambda q\dot{n}\delta n\right]\mathrm{d}V, \tag{7a}$$

$$\delta W_{(i)} = \int_V \left[T_{ij}\delta S_{ij} + \tau_{ijk}\delta\eta_{ijk} - D_i\delta E_i + \lambda J_i^n \delta N_i\right]\mathrm{d}V, \tag{7b}$$

with V being the region occupied by the structure; ρ stands for mass density; λ is a constant satisfying all terms related to concentrations of charge carriers; f_i is the mechanical body force. The first- and second-time derivatives are represented by the overhead "$\cdot$" and "$\cdot\cdot$" in this instance and the sequel (i.e., $\dot{u}_i = \partial u_i/\partial t$, $\ddot{u}_i = \partial^2 u_i/\partial t^2$).

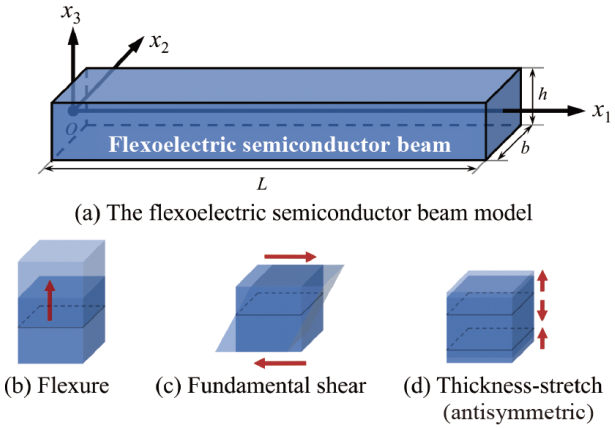

(a) The flexoelectric semiconductor beam model

(b) Flexure (c) Fundamental shear (d) Thickness-stretch (antisymmetric)

Figure 1 FS beam and corresponding deformation modes.

Using Eqs. (4) and (5) into Eq. (7a) gives

$$\begin{aligned}\delta W_{(d)} = -\int_0^L \big[&(f_1^{(1)} - \rho^{(2)}\ddot{u}_1^{(1)})\delta u_1^{(1)} \\ &+ (f_3^{(0)} - \rho^{(0)}\ddot{u}_3^{(0)} - \rho^{(2)}\ddot{u}_3^{(2)})\delta u_3^{(0)} \\ &+ (f_3^{(2)} - \rho^{(2)}\ddot{u}_3^{(0)} - \rho^{(4)}\ddot{u}_3^{(2)})\delta u_3^{(2)} \\ &+ q^{(2)}n^{(1)}\delta\varphi^{(1)} - \lambda q^{(2)}\dot{n}^{(1)}\delta n^{(1)}\big]\mathrm{d}x_1,\end{aligned} \tag{8}$$

where

$$\begin{aligned}\left[f_1^{(m)}, f_3^{(m)}\right] &= \int_A x_3^m [f_1, f_3]\mathrm{d}A, \\ \rho^{(m)} &= \int_A x_3^m \rho\mathrm{d}A, \\ q^{(m)} &= \int_A x_3^m q\mathrm{d}A, \quad m = 0, 1, 2, \ldots\end{aligned} \tag{9}$$

are the body force, mass density, and elementary charge resultants across the cross-section area A of the beam, respectively.

According to Eqs. (2), (4), (5), and (7b), we have

$$\begin{aligned}\delta W_{(i)} = -\int_0^L \big[&\left(T_{11,1}^{(1)} - T_{13}^{(0)} + \tau_{113,1}^{(0)} + \tau_{131,1}^{(0)} - \tau_{111,11}^{(1)}\right)\delta u_1^{(1)} \\ &+ \left(T_{13,1}^{(0)} - \tau_{131,11}^{(0)}\right)\delta u_3^{(0)} + \left(T_{13,1}^{(2)} - 2T_{33}^{(1)} - 2\tau_{333}^{(0)} + 2\tau_{133,1}^{(1)}\right. \\ &\left. + 2\tau_{331,1}^{(1)} - \tau_{131,11}^{(2)}\right)\delta u_3^{(2)} + \left(D_{1,1}^{(1)} - D_3^{(0)}\right)\delta\varphi^{(1)} \\ &+ \lambda\left(J_{1,1}^{n(1)} - J_3^{n(0)}\right)\delta n^{(1)}\big]\mathrm{d}x_1 \\ &+ \Big[\left(T_{11}^{(1)} + \tau_{113}^{(0)} + \tau_{131}^{(0)} - \tau_{111,1}^{(1)}\right)\delta u_1^{(1)} \\ &+ \left(T_{13}^{(0)} - \tau_{131,1}^{(0)}\right)\delta u_3^{(0)} + \left(T_{13}^{(2)} + 2\tau_{133}^{(1)} + 2\tau_{331}^{(1)} - \tau_{131,1}^{(2)}\right) \\ &\cdot\delta u_3^{(2)} + \tau_{111}^{(1)}\delta u_{1,1}^{(1)} + \tau_{131}^{(0)}\delta u_{3,1}^{(0)} + \tau_{131}^{(2)}\delta u_{3,1}^{(2)} \\ &+ D_1^{(1)}\delta\varphi^{(1)} + \lambda J_1^{n(1)}\delta n^{(1)}\Big]\Big|_0^L,\end{aligned} \tag{10}$$

where

$$T_{ij}^{(m)}=\int_A x_3^m T_{ij}\mathrm{d}A,\quad \tau_{ijk}^{(m)}=\int_A x_3^m \tau_{ijk}\mathrm{d}A,$$
$$D_i^{(m)}=\int_A x_3^m D_i\mathrm{d}A,\quad J_i^{n(m)}=\int_A x_3^m J_i^n\mathrm{d}A, \tag{11}$$

are the stress, higher-order stress, electric displacement, and electron electric current resultants on the beam cross-section, respectively.

Substituting Eqs. (8) and (10) into Eq. (6) and applying the fundamental lemma of the calculus of variations results in

$$\begin{cases} T_{13,1}^{(0)}-\tau_{131,11}^{(0)}+f_3^{(0)}=\rho^{(0)}\ddot{u}_3^{(0)}+\rho^{(2)}\ddot{u}_3^{(2)},\\ T_{11,1}^{(1)}-T_{13}^{(0)}+\tau_{113,1}^{(0)}+\tau_{131,1}^{(0)}-\tau_{111,11}^{(1)}+f_1^{(1)}=\rho^{(2)}\ddot{u}_1^{(1)},\\ T_{13,1}^{(2)}-2T_{33}^{(1)}-2\tau_{333}^{(0)}+2\tau_{133,1}^{(1)}+2\tau_{331,1}^{(1)}-\tau_{131,11}^{(2)}+f_3^{(2)}\\ =\rho^{(2)}\ddot{u}_3^{(0)}+\rho^{(4)}\ddot{u}_3^{(2)},\\ D_{1,1}^{(1)}-D_3^{(0)}=-q^{(2)}n^{(1)},\\ J_{1,1}^{n(1)}-J_3^{n(0)}=q^{(2)}\dot{n}^{(1)}. \end{cases} \tag{12}$$

Note that Eq. (12) represents the coupled field equations for the established FS beam model. These equations hold true at any moment inside the temporal interval $[t_0, t_1]$. The associated BCs are given as

$$\begin{cases} T_{13}^{(0)}-\tau_{131,1}^{(0)}=0\quad\text{or}\quad u_3^{(0)}=\overline{u}_3^{(0)},\\ T_{11}^{(1)}+\tau_{113}^{(0)}+\tau_{131}^{(0)}-\tau_{111,1}^{(1)}=0\quad\text{or}\quad u_1^{(1)}=\overline{u}_1^{(1)},\\ T_{13}^{(2)}+2\tau_{133}^{(1)}+2\tau_{331}^{(1)}-\tau_{131,1}^{(2)}=0\quad\text{or}\quad u_3^{(2)}=\overline{u}_3^{(2)},\\ \tau_{111}^{(1)}=0\quad\text{or}\quad u_{1,1}^{(1)}=\overline{u}_{1,1}^{(1)},\\ \tau_{131}^{(0)}=0\quad\text{or}\quad u_{3,1}^{(0)}=\overline{u}_{3,1}^{(0)},\\ \tau_{131}^{(2)}=0\quad\text{or}\quad u_{3,1}^{(2)}=\overline{u}_{3,1}^{(2)},\\ D_1^{(1)}=0\quad\text{or}\quad \varphi^{(1)}=\overline{\varphi}^{(1)},\\ J_1^{n(1)}=0\quad\text{or}\quad n^{(1)}=\overline{n}^{(1)}, \end{cases} \tag{13}$$

with the overhead bars representing the prescribed value. For specific constraints, natural BCs or essential BCs can be chosen from these general options.

It is vital to emphasize that the field Eq. (12) and the BCs (13) are applicable to arbitrarily anisotropic FS beams. In the subsequent development, the beam is taken to be made from a centrosymmetric semiconductor with m3m point group. Then, on the basis of material matrices provided in Appendix A, the constitutive relations in terms of field variables can be obtained as

$$\begin{aligned} T_{11}&=c_{11}x_3u_{1,1}^{(1)}+2c_{12}x_3u_3^{(2)},\\ T_{33}&=c_{12}x_3u_{1,1}^{(1)}+2c_{11}x_3u_3^{(2)},\\ T_{13}&=c_{44}\left(u_1^{(1)}+u_{3,1}^{(0)}+x_3^2u_{3,1}^{(2)}\right), \end{aligned} \tag{14}$$

$$\begin{aligned} \tau_{111}&=\ell^2c_{11}x_3u_{1,11}^{(1)}+2\ell^2c_{12}x_3u_{3,1}^{(2)}+f_{11}x_3\varphi_{,1}^{(1)},\\ \tau_{113}&=\ell^2c_{11}u_{1,1}^{(1)}+2\ell^2c_{12}u_3^{(2)}+f_{14}\varphi^{(1)},\\ \tau_{331}&=\ell^2c_{12}x_3u_{1,11}^{(1)}+2\ell^2c_{11}x_3u_{3,1}^{(2)}+f_{14}x_3\varphi_{,1}^{(1)},\\ \tau_{333}&=\ell^2c_{12}u_{1,1}^{(1)}+2\ell^2c_{11}u_3^{(2)}+f_{11}\varphi^{(1)},\\ \tau_{131}&=\ell^2c_{44}(u_{1,1}^{(1)}+u_{3,11}^{(0)}+x_3^2u_{3,11}^{(2)})+f_{111}\varphi^{(1)},\\ \tau_{133}&=2\ell^2c_{44}x_3u_{3,1}^{(2)}+f_{111}x_3\varphi_{,1}^{(1)}, \end{aligned} \tag{15}$$

$$\begin{aligned} D_1&=-\varepsilon_{11}x_3\varphi_{,1}^{(1)}+f_{11}x_3u_{1,11}^{(1)}+2f_{111}x_3u_{3,1}^{(2)}+2f_{14}x_3u_{3,1}^{(2)},\\ D_3&=-\varepsilon_{11}\varphi^{(1)}+2f_{11}u_3^{(2)}+f_{111}\left(u_{1,1}^{(1)}+u_{3,11}^{(0)}+x_3^2u_{3,11}^{(2)}\right)+f_{14}u_{1,1}^{(1)}, \end{aligned} \tag{16}$$

$$\begin{aligned} J_1^n&=-qn_0\mu_{11}^n x_3\varphi_{,1}^{(1)}+qD_{11}^n x_3n_{,1}^{(1)},\\ J_3^n&=-qn_0\mu_{11}^n\varphi^{(1)}+qD_{11}^n n^{(1)}. \end{aligned} \tag{17}$$

Note that in Eq. (15), the relation $g_{ijklmn}=\ell^2c_{ijlm}\delta_{kn}$ is employed through simplifying the general form of the strain gradient theory [53], as demonstrated by Altan and Aifantis [54]. Here, ℓ denotes the sole length scale parameter that adequately captures the microstructure effect.

Substituting Eqs. (14)-(17) into Eq. (11), the corresponding resultants may be written in terms of $u_3^{(0)}$, $u_1^{(1)}$, $u_3^{(2)}$, $\varphi^{(1)}$, and $n^{(1)}$, i.e.,

$$\begin{aligned} T_{13}^{(0)}&=c_{44}\left[A\left(u_1^{(1)}+u_{3,1}^{(0)}\right)+I_2u_{3,1}^{(2)}\right],\\ T_{11}^{(1)}&=I_2\left(c_{11}u_{1,1}^{(1)}+2c_{12}u_3^{(2)}\right),\\ T_{33}^{(1)}&=I_2\left(c_{12}u_{1,1}^{(1)}+2c_{11}u_3^{(2)}\right),\\ T_{13}^{(2)}&=c_{44}\left[I_2\left(u_1^{(1)}+u_{3,1}^{(0)}\right)+I_4u_{3,1}^{(2)}\right], \end{aligned} \tag{18}$$

$$\begin{aligned} \tau_{113}^{(0)}&=A\left(\ell^2c_{11}u_{1,1}^{(1)}+2\ell^2c_{12}u_3^{(2)}+f_{14}\varphi^{(1)}\right),\\ \tau_{333}^{(0)}&=A\left(\ell^2c_{12}u_{1,1}^{(1)}+2\ell^2c_{11}u_3^{(2)}+f_{11}\varphi^{(1)}\right),\\ \tau_{131}^{(0)}&=\ell^2c_{44}\left[I_0\left(u_{1,1}^{(1)}+u_{3,11}^{(0)}\right)+I_2u_{3,11}^{(2)})\right]+Af_{111}\varphi^{(1)},\\ \tau_{111}^{(1)}&=I_2\left(\ell^2c_{11}u_{1,11}^{(1)}+2\ell^2c_{12}u_{3,1}^{(2)}+f_{11}\varphi_{,1}^{(1)}\right),\\ \tau_{331}^{(1)}&=I_2\left(\ell^2c_{12}u_{1,11}^{(1)}+2\ell^2c_{11}u_{3,1}^{(2)}+f_{14}\varphi_{,1}^{(1)}\right),\\ \tau_{133}^{(1)}&=I_2\left(2\ell^2c_{44}u_{3,1}^{(2)}+f_{111}\varphi_{,1}^{(1)}\right),\\ \tau_{131}^{(2)}&=\ell^2c_{44}\left[I_2\left(u_{1,1}^{(1)}+u_{3,11}^{(0)}\right)+I_4u_{3,11}^{(2)}\right]+I_2f_{111}\varphi^{(1)}, \end{aligned} \tag{19}$$

$$\begin{aligned} D_3^{(0)}&=A\left[-\varepsilon_{11}\varphi^{(1)}+2f_{11}u_3^{(2)}+f_{111}\left(u_{1,1}^{(1)}+u_{3,11}^{(0)}\right)+f_{14}u_{1,1}^{(1)}\right]\\ &\quad+I_2f_{111}u_{3,11}^{(2)},\\ D_1^{(1)}&=I_2\left(-\varepsilon_{11}\varphi_{,1}^{(1)}+f_{11}u_{1,11}^{(1)}+2f_{111}u_{3,1}^{(2)}+2f_{14}u_{3,1}^{(2)}\right), \end{aligned} \tag{20}$$

$$J_1^{n(1)} = -q^{(2)} n_0 \mu_{11}^n \varphi_{,1}^{(1)} + q^{(2)} D_{11}^n n_{,1}^{(1)},$$
$$J_3^{n(0)} = -q^{(0)} n_0 \mu_{11}^n \varphi^{(1)} + q^{(0)} D_{11}^n n^{(1)}, \tag{21}$$

where $I_2 = bh^3/12$ and $I_4 = bh^5/80$ represent the second and fourth moment of area, respectively.

Using Eqs. (18)-(21) in Eq. (12) then leads to the governing equations for the proposed FS beam as

$$\begin{aligned}
&c_{44}\left[A\left(u_{1,1}^{(1)} + u_{3,11}^{(0)}\right) + I_2 u_{3,11}^{(2)}\right] \\
&-\ell^2 c_{44}\left[A\left(u_{1,111}^{(1)} + u_{3,1111}^{(0)}\right) + I_2 u_{3,1111}^{(2)}\right] \\
&-A f_{111}\varphi_{,11}^{(1)} + f_3^{(0)} = \rho^{(0)} \ddot{u}_3^{(0)} + \rho^{(2)} \ddot{u}_3^{(2)},
\end{aligned} \tag{22a}$$

$$\begin{aligned}
&I_2\left(c_{11} u_{1,11}^{(1)} + 2c_{12} u_{3,1}^{(2)}\right) - c_{44}\left[A\left(u_1^{(1)} + u_{3,1}^{(0)}\right) + I_2 u_{3,1}^{(2)}\right] \\
&+A\left(\ell^2 c_{11} u_{1,11}^{(1)} + 2\ell^2 c_{12} u_{3,1}^{(2)} + f_{14}\varphi_{,1}^{(1)}\right) \\
&+\ell^2 c_{44}\left[A\left(u_{1,11}^{(1)} + u_{3,111}^{(0)}\right) + I_2 u_{3,111}^{(2)}\right] \\
&+A f_{111}\varphi_{,1}^{(1)} - I_2\left(\ell^2 c_{11} u_{1,1111}^{(1)} + 2\ell^2 c_{12} u_{3,111}^{(2)} + f_{11}\varphi_{,111}^{(1)}\right) + f_1^{(1)} \\
&= \rho^{(2)} \ddot{u}_1^{(1)},
\end{aligned} \tag{22b}$$

$$\begin{aligned}
&c_{44}\left[I_2\left(u_{1,1}^{(1)} + u_{3,11}^{(0)}\right) + I_4 u_{3,11}^{(2)}\right] - 2I_2\left(c_{12} u_{1,1}^{(1)} + 2c_{11} u_3^{(2)}\right) \\
&-2A\left(\ell^2 c_{12} u_{1,1}^{(1)} + 2\ell^2 c_{11} u_3^{(2)} + f_{11}\varphi^{(1)}\right) \\
&+2I_2\left(2\ell^2 c_{44} u_{3,11}^{(2)} + f_{111}\varphi_{,11}^{(1)}\right) \\
&+2I_2\left(\ell^2 c_{12} u_{1,111}^{(1)} + 2\ell^2 c_{11} u_{3,11}^{(2)} + f_{14}\varphi_{,11}^{(1)}\right) \\
&-\ell^2 c_{44}\left[I_2\left(u_{1,111}^{(1)} + u_{3,1111}^{(0)}\right) + I_4 u_{3,1111}^{(2)}\right] - I_2 f_{111}\varphi_{,11}^{(1)} + f_3^{(2)} \\
&= \rho^{(2)} \ddot{u}_3^{(0)} + \rho^{(4)} \ddot{u}_3^{(2)},
\end{aligned} \tag{22c}$$

$$\begin{aligned}
&I_2\left(-\varepsilon_{11}\varphi_{,11}^{(1)} + f_{11} u_{1,111}^{(1)} + f_{111} u_{3,11}^{(2)} + 2f_{14} u_{3,11}^{(2)}\right) \\
&-A\left[-\varepsilon_{11}\varphi^{(1)} + 2f_{11} u_3^{(2)} + f_{111}\left(u_{1,1}^{(1)} + u_{3,11}^{(0)}\right) + f_{14} u_{1,1}^{(1)}\right] \\
&= -q^{(2)} n^{(1)},
\end{aligned} \tag{22d}$$

$$\begin{aligned}
&-q^{(2)} n_0 \mu_{11}^n \varphi_{,11}^{(1)} + q^{(2)} D_{11}^n n_{,11}^{(1)} + q^{(0)} n_0 \mu_{11}^n \varphi^{(1)} - q^{(0)} D_{11}^n n^{(1)} \\
&= q^{(2)} \dot{n}^{(1)}.
\end{aligned} \tag{22e}$$

The governing equations in Eqs. (22a)-(22e), together with the related BCs described in Eq. (13), formally define the boundary-initial value problem for determining $u_3^{(0)}$, $u_1^{(1)}$, $u_3^{(2)}$, $\varphi^{(1)}$, and $n^{(1)}$. Furthermore, this issue requires initial conditions to be provided at instance $t = 0$. By disregarding the antisymmetric thickness-stretch deformation $u_3^{(2)}$, Eqs. (22a)-(22e) reduce to

$$\begin{aligned}
&c_{44} A\left(u_{1,1}^{(1)} + u_{3,11}^{(0)}\right) - \ell^2 c_{44} A\left(u_{1,111}^{(1)} + u_{3,1111}^{(0)}\right) \\
&-A f_{111}\varphi_{,11}^{(1)} + f_3^{(0)} = \rho^{(0)} \ddot{u}_3^{(0)}, \\
&I_2 c_{11} u_{1,11}^{(1)} - c_{44} A\left(u_1^{(1)} + u_{3,1}^{(0)}\right) + A\left(\ell^2 c_{11} u_{1,11}^{(1)} + f_{14}\varphi_{,1}^{(1)}\right) \\
&+\ell^2 c_{44} A\left(u_{1,11}^{(1)} + u_{3,111}^{(0)}\right) + A f_{111}\varphi_{,1}^{(1)} \\
&-I_2\left(\ell^2 c_{11} u_{1,1111}^{(1)} + f_{11}\varphi_{,111}^{(1)}\right) + f_1^{(1)} = \rho^{(2)} \ddot{u}_1^{(1)}, \\
&I_2\left(-\varepsilon_{11}\varphi_{,11}^{(1)} + f_{11} u_{1,111}^{(1)}\right) \\
&-A\left[-\varepsilon_{11}\varphi^{(1)} + f_{111}\left(u_{1,1}^{(1)} + u_{3,11}^{(0)}\right) + f_{14} u_{1,1}^{(1)}\right] \\
&= -q^{(2)} n^{(1)}, \\
&-q^{(2)} n_0 \mu_{11}^n \varphi_{,11}^{(1)} + q^{(2)} D_{11}^n n_{,11}^{(1)} + q^{(0)} n_0 \mu_{11}^n \varphi^{(1)} \\
&-q^{(0)} D_{11}^n n^{(1)} = q^{(2)} \dot{n}^{(1)},
\end{aligned} \tag{23}$$

which is a Timoshenko beam model that incorporates microstructure, flexoelectric, and semiconductor effects.

Furthermore, we introduce several non-dimensional variables as follows:

$$\begin{aligned}
&X = x_1/h, \quad U_3^{(0)} = u_3^{(0)}/h, \quad U_1^{(1)} = u_1^{(1)}, \\
&U_3^{(2)} = h u_3^{(2)}, \quad \varphi_T = D_{11}^n/\mu_{11}^n, \quad \psi = h\varphi^{(1)}/\varphi_T, \\
&N = h n^{(1)}/n_0, \quad \tau = t/T,
\end{aligned} \tag{24}$$

where T is an arbitrary time interval. Hence, the non-dimensional governing equations become

$$\begin{aligned}
&\mathbb{A}_1 U_{3,XX}^{(0)} + \mathbb{A}_2 U_{3,XXXX}^{(0)} + \mathbb{A}_3 U_{1,X}^{(1)} + \mathbb{A}_4 U_{1,XXX}^{(1)} + \mathbb{A}_5 U_{3,XX}^{(2)} \\
&+\mathbb{A}_6 U_{3,XXXX}^{(2)} + \mathbb{A}_7 \psi_{,XX} + \mathbb{F}_1 = \mathbb{M}_1 U_{3,\tau\tau}^{(0)} + \mathbb{M}_2 U_{3,\tau\tau}^{(2)},
\end{aligned} \tag{25a}$$

$$\begin{aligned}
&\mathbb{B}_1 U_{3,X}^{(0)} + \mathbb{B}_2 U_{3,XXX}^{(0)} + \mathbb{B}_3 U_1^{(1)} + \mathbb{B}_4 U_{1,XX}^{(1)} + \mathbb{B}_5 U_{1,XXXX}^{(1)} \\
&+\mathbb{B}_6 U_{3,X}^{(2)} + \mathbb{B}_7 U_{3,XXX}^{(2)} + \mathbb{B}_8 \psi_{,X} + \mathbb{B}_9 \psi_{,XXX} + \mathbb{F}_2 = \mathbb{M}_3 U_{1,\tau\tau}^{(1)},
\end{aligned} \tag{25b}$$

$$\begin{aligned}
&\mathbb{C}_1 U_{3,XX}^{(0)} + \mathbb{C}_2 U_{3,XXXX}^{(0)} + \mathbb{C}_3 U_{1,X}^{(1)} + \mathbb{C}_4 U_{1,XXX}^{(1)} \\
&+\mathbb{C}_5 U_3^{(2)} + \mathbb{C}_6 U_{3,XX}^{(2)} + \mathbb{C}_7 U_{3,XXXX}^{(2)} + \mathbb{C}_8 \psi \\
&+\mathbb{C}_9 \psi_{,XX} + \mathbb{F}_3 = \mathbb{M}_4 U_{3,\tau\tau}^{(0)} + \mathbb{M}_5 U_{3,\tau\tau}^{(2)},
\end{aligned} \tag{25c}$$

$$\begin{aligned}
&\mathbb{D}_1 U_{3,XX}^{(0)} + \mathbb{D}_2 U_{1,X}^{(1)} + \mathbb{D}_3 U_{1,XXX}^{(1)} + \mathbb{D}_4 U_3^{(2)} + \mathbb{D}_5 U_{3,XX}^{(2)} \\
&+\mathbb{D}_6 \psi + \mathbb{D}_7 \psi_{,XX} + \mathbb{D}_8 N = 0,
\end{aligned} \tag{25d}$$

$$\mathbb{E}_1 \psi + \mathbb{E}_2 \psi_{,XX} + \mathbb{E}_3 N + \mathbb{E}_4 N_{,XX} = \mathbb{M}_6 N_{,\tau}, \tag{25e}$$

where the nondimensional coefficients are

$$\begin{aligned}
&[\mathbb{A}_1, \mathbb{A}_2, \mathbb{A}_3, \mathbb{A}_4, \mathbb{A}_5, \mathbb{A}_6, \mathbb{A}_7, \mathbb{F}_1] \\
&= \left[1, -\frac{\ell^2}{h^2}, 1, -\frac{\ell^2}{h^2}, \frac{I_2}{Ah^2}, -\frac{\ell^2 I_2}{Ah^4}, -\frac{f_{111}\varphi_T}{c_{44}h^2}, \frac{h f_3^{(0)}}{c_{44}A}\right],
\end{aligned} \tag{26a}$$

$$
\begin{aligned}
&[\mathbb{B}_1,\mathbb{B}_2,\mathbb{B}_3,\mathbb{B}_4,\mathbb{B}_5,\mathbb{B}_6,\mathbb{B}_7,\mathbb{B}_8,\mathbb{B}_9,\mathbb{F}_2]\\
&=\Bigg[-1,\frac{\ell^2}{h^2},-1,\frac{\ell^2(c_{11}+c_{44})A+c_{11}I_2}{c_{44}Ah^2},-\frac{\ell^2c_{11}I_2}{c_{44}Ah^4},\\
&\frac{(2c_{12}-c_{44})I_2+2\ell^2c_{12}A}{c_{44}Ah^2},\frac{\ell^2(c_{44}-2c_{12})I_2}{c_{44}Ah^4},\\
&\frac{(f_{14}+f_{111})\varphi_T}{c_{44}h^2},-\frac{I_2f_{11}\varphi_T}{c_{44}Ah^4},\frac{f_1^{(1)}}{c_{44}A}\Bigg],
\end{aligned}
\tag{26b}
$$

$$
\begin{aligned}
&[\mathbb{C}_1,\mathbb{C}_2,\mathbb{C}_3,\mathbb{C}_4,\mathbb{C}_5,\mathbb{C}_6,\mathbb{C}_7,\mathbb{C}_8,\mathbb{C}_9,\mathbb{F}_3]\\
&=\Bigg[1,-\frac{\ell^2}{h^2},\frac{(c_{44}-2c_{12})I_2-2\ell^2c_{12}A}{c_{44}I_2},\frac{\ell^2(2c_{12}-c_{44})}{c_{44}h^2},\\
&-\frac{4c_{11}(\ell^2A+I_2)}{c_{44}I_2},\frac{c_{44}I_4+4\ell^2I_2(c_{11}+c_{44})}{c_{44}I_2h^2},-\frac{\ell^2I_4}{I_2h^4},\\
&-\frac{2f_{11}A\varphi_T}{c_{44}I_2},\frac{(f_{111}+2f_{14})\varphi_T}{c_{44}h^2},\frac{hf_3^{(2)}}{c_{44}I_2}\Bigg],
\end{aligned}
\tag{26c}
$$

$$
\begin{aligned}
&[\mathbb{D}_1,\mathbb{D}_2,\mathbb{D}_3,\mathbb{D}_4,\mathbb{D}_5,\mathbb{D}_6,\mathbb{D}_7,\mathbb{D}_8]\\
&=\Bigg[-1,-1-\frac{f_{14}}{f_{111}},\frac{f_{11}I_2}{f_{111}Ah^2},-\frac{2f_{11}}{f_{111}},\frac{I_2}{Ah^2}+\frac{2f_{14}I_2}{f_{111}Ah^2},\\
&\frac{\varepsilon_{11}\varphi_T}{f_{111}},-\frac{\varepsilon_{11}\varphi_TI_2}{f_{111}Ah^2},\frac{q^{(2)}n_0}{f_{111}A}\Bigg],
\end{aligned}
\tag{26d}
$$

$$
[\mathbb{E}_1,\mathbb{E}_2,\mathbb{E}_3,\mathbb{E}_4]=\Bigg[1,-\frac{q^{(2)}}{q^{(0)}h^2},-1,\frac{q^{(2)}}{q^{(0)}h^2}\Bigg],
\tag{26e}
$$

$$
\begin{aligned}
&[\mathbb{M}_1,\mathbb{M}_2,\mathbb{M}_3,\mathbb{M}_4,\mathbb{M}_5,\mathbb{M}_6]\\
&=\Bigg[\frac{\rho^{(0)}h^2}{c_{44}AT^2},\frac{\rho^{(2)}}{c_{44}AT^2},\frac{\rho^{(2)}}{c_{44}AT^2},\frac{\rho^{(2)}h^2}{c_{44}I_2T^2},\frac{\rho^{(4)}}{c_{44}I_2T^2},\frac{q^{(2)}}{q^{(0)}D_{11}^nT}\Bigg].
\end{aligned}
\tag{26f}
$$

3. Examples: static bending and wave propagation analyses

To comprehensively investigate the role of antisymmetric thickness-stretch in the FS nanobeam model developed in the previous section, two sample problems addressing different aspects are examined here. One involves the static bending of a simply supported FS beam induced by uniform pressure, and the other examines the wave motions in an unbounded FS beam. Together, these problems provide a detailed description of electromechanical interactions in the FS nanobeam when antisymmetric thickness-stretch is taken into account.

3.1 Static bending

According to Eq. (13), the specific BCs at $x_1 = 0$ and $x_1 = L$ for a simply supported FS beam associated with Ohmic contact conditions (see Fig. 2) are

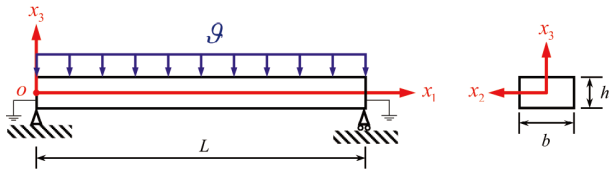

Figure 2 Sketch of a simply supported FS beam and the coordinate system.

$$u_3^{(0)}=0, \tag{27a}$$

$$T_{11}^{(1)}+\tau_{113}^{(0)}+\tau_{131}^{(0)}-\tau_{111,1}^{(1)}=0, \tag{27b}$$

$$u_3^{(2)}=0, \tag{27c}$$

$$u_{1,1}^{(1)}=0, \tag{27d}$$

$$\tau_{131}^{(0)}=0, \tag{27e}$$

$$\tau_{131}^{(2)}=0, \tag{27f}$$

$$\varphi^{(1)}=0, \tag{27g}$$

$$n^{(1)}=0. \tag{27h}$$

Using Eqs. (18) and (19) in Eqs. (27b), (27e), (27f) yields

$$
\begin{aligned}
&I_2\left(c_{11}u_{1,1}^{(1)}+2c_{12}u_3^{(2)}\right)+A\left(\ell^2c_{11}u_{1,1}^{(1)}+2\ell^2c_{12}u_3^{(2)}+f_{14}\varphi^{(1)}\right)\\
&+\ell^2c_{44}\left[A\left(u_{1,1}^{(1)}+u_{3,11}^{(0)}\right)+I_2u_{3,11}^{(2)}\right]+Af_{111}\varphi^{(1)}\\
&-I_2\left(\ell^2c_{11}u_{1,111}^{(1)}+2\ell^2c_{12}u_{3,11}^{(2)}+f_{11}\varphi_{11}^{(1)}\right)=0,\\
&\ell^2c_{44}\left[A\left(u_{1,1}^{(1)}+u_{3,11}^{(0)}\right)+I_2u_{3,11}^{(2)}\right)\right]+Af_{111}\varphi^{(1)}=0,\\
&\ell^2c_{44}\left[I_2\left(u_{1,1}^{(1)}+u_{3,11}^{(0)}\right)+I_4u_{3,11}^{(2)}\right]+I_2f_{111}\varphi^{(1)}=0.
\end{aligned}
\tag{28}
$$

The non-dimensional BCs are

$$
\begin{aligned}
&\frac{\ell^2c_{44}A}{h}U_{3,XX}^{(0)}+\frac{c_{11}I_2+\ell^2(c_{11}+c_{44})A}{h}U_{1,X}^{(1)}-\frac{\ell^2c_{11}I_2}{h^3}U_{1,XXX}^{(1)}\\
&+\frac{2c_{12}(\ell^2A+I_2)}{h}U_3^{(2)}+\frac{\ell^2(c_{44}-2c_{12})I_2}{h^3}U_{3,XX}^{(2)}\\
&+\frac{(f_{14}+f_{111})AD_{11}^n}{\mu_{11}^nh}\psi-\frac{f_{11}I_2D_{11}^n}{\mu_{11}^nh^3}\psi_{,XX}=0,\\
&\left(U_{1,X}^{(1)}+U_{3,XX}^{(0)}\right)+\frac{I_2}{Ah^2}U_{3,XX}^{(2)}+\frac{f_{111}\varphi_T}{\ell^2c_{44}}\psi=0,\\
&\left(U_{1,X}^{(1)}+U_{3,XX}^{(0)}\right)+\frac{I_4}{I_2h^2}U_{3,XX}^{(2)}+\frac{f_{111}\varphi_T}{\ell^2c_{44}}\psi=0,\\
&U_3^{(0)}=0,\quad U_3^{(2)}=0,\quad \psi=0,\quad N=0,\\
&\text{at}\quad X=0\quad\text{and}\quad L/h.
\end{aligned}
\tag{29}
$$

In the case of static bending, a uniformly transverse load ϑ (i.e., $f_3^{(0)}=\vartheta$) is exerted on the upper surface of the beam, while other body forces and all the time derivatives vanish. Then the boundary value problem can be analytically addressed using the subsequent Fourier series solutions:

$$\left\{U_3^{(0)}, U_3^{(2)}, \psi, N\right\} = \sum_{k=1}^{\infty}\{\mathbb{W}_k, \mathbb{S}_k, \mathbb{Y}_k, \mathbb{N}_k\}\sin(\xi_k X),$$
$$U_1^{(1)} = \sum_{k=1}^{\infty}\mathbb{V}_k\cos(\xi_k X), \tag{30}$$

where $\xi_k = k\pi h/L$; $\mathbb{W}_k$, $\mathbb{V}_k$, $\mathbb{S}_k$, $\mathbb{Y}_k$, and $\mathbb{N}_k$ are the unknown Fourier coefficients. It can be easily seen that $U_3^{(0)}$, $U_1^{(1)}$, $U_3^{(2)}$, ψ, and N satisfy the BCs in Eq. (29) for any $\mathbb{W}_k$, $\mathbb{V}_k$, $\mathbb{S}_k$, $\mathbb{Y}_k$, and $\mathbb{N}_k$. The non-dimensional mechanical load $\mathbb{F}_1$ in Eq. (25a) can similarly be expanded as

$$\mathbb{F}_1 = \sum_{k=1}^{\infty}\mathbb{Q}_k\sin(\xi_k X), \tag{31a}$$

$$\mathbb{Q}_k = \frac{2h\vartheta}{kc_{44}A\pi}[1-\cos(k\pi)]. \tag{31b}$$

Inserting Eqs. (30) and (31a) into Eqs. (25a)-(25e) yieds

$$[K_{ij}][\mathbb{W}_k, \mathbb{V}_k, \mathbb{S}_k, \mathbb{Y}_k, \mathbb{N}_k]^{\mathrm{T}} = [-\mathbb{Q}_k, 0, 0, 0, 0]^{\mathrm{T}}, \tag{32}$$

where $[K_{ij}]$ is a 5 × 5 matrix detailed in Eq. (B1) in Appendix B. By solving the system of Eq. (32) will yield $\mathbb{W}_k, \mathbb{V}_k, \mathbb{S}_k, \mathbb{Y}_k, \mathbb{N}_k$. These can then be substituted into Eq. (30) to derive the accurate solutions of $U_3^{(0)}$, $U_1^{(1)}$, $U_3^{(2)}$, ψ, and N in the static bending issue of the simply supported FS beam displayed in Fig. 2.

For illustrative purposes, the geometrical parameters of the nanobeam are considered to be moderately thick with h = 20 nm, $b = 2h$, and $L = 5h$. The beam is chosen to be silicon. The mass density, elastic constants, dielectric coefficient, electron mobility, and diffusion constant are provided in Sze and Ng's work [55]. The flexoelectric coefficients are f_{11} = 1.3 nC/m and $f_{14} = f_{111}$ = 0.4 nC/m [39].

The total terms present in each expansion within Eq. (30) can be regulated by adjusting the parameter k, necessitating a convergence analysis. To ensure that the analytical solution is accurate enough, the charge accumulation amount Q on the upper half of the beam ($Q = b\int_0^L \mathrm{d}x_1\int_0^{\frac{h}{2}} q\Delta n\mathrm{d}x_3$) varying with k is calculated. It is found that the numerical results obtained with k = 25 are identical to those calculated with higher k values (up to k = 40), matching the third decimal place for Q (= –8.654 × 10^{-23} C). Considering the linear coupling relationship between mechanical displacements, electric potential, and electron concentration perturbation within the beam, as well as the correspondence between Q and Δn, it can be concluded that utilizing the first 25 terms in Eq. (30) is adequate for the convergence of all the field variables.

We place greater emphasis on the effect of the antisymmetric thickness-stretch of the beam on electromechanical interactions. Figure 3(a) and (b) illustrates the bending and fundamental thickness-shear at the top surface of the beam where $x_3 = h/2$. It can be observed that when $u_3^{(2)}$ is excluded (Timoshenko beam model), both bending and fundamental thickness-shear deformations slightly diminish compared to those in the current beam model.

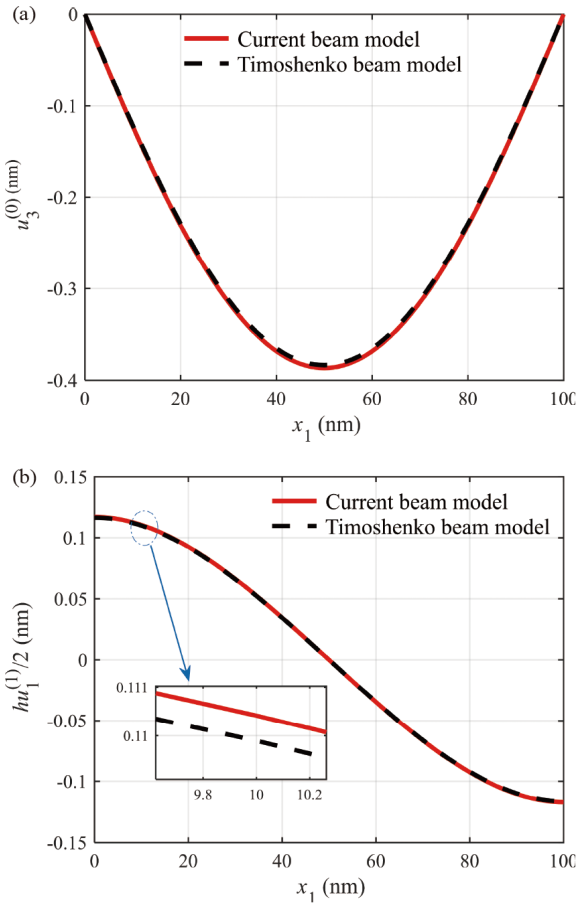

Figure 3 Effect of antisymmetric thickness-stretch on (a) bending and (b) fundamental thickness-shear ($\ell = 1 \times 10^{-9}$ m, $n_0 = 1 \times 10^{21}$ m^{-3}, ϑ = 1 N/m).

Figure 4(a) and (b) depicts the electron concentration perturbation Δn of the FS beam in a 3D view, resulting from the uniformly distributed stress ϑ. It is evident that electrons fluctuate towards the bottom of the beam, resulting in a negative charge accumulation in that area. Along the same cross-section, charge redistribution displays antisymmetry across the neutral layer of the beam. The charge carriers exhibit near uniformity along the surfaces of the FS beam, making it easy to drain or inject via top and bottom electrodes when serving as a circuit element. The resulting numerical findings provide valuable insights for elucidating the mechanism of charge redistribution within the FS beam.

Furthermore, it is showcased that the concentration perturbation of electrons predicted by the two beam models differ significantly (with a discrepancy of more than tenfold), indicating that the flexoelectric polarization produced by $u_3^{(2)}$ is much greater than that of $u_3^{(0)}$ but in the opposite direction. This underscores the importance of incorporating antisymmetric thickness-stretch in the examination of flex-

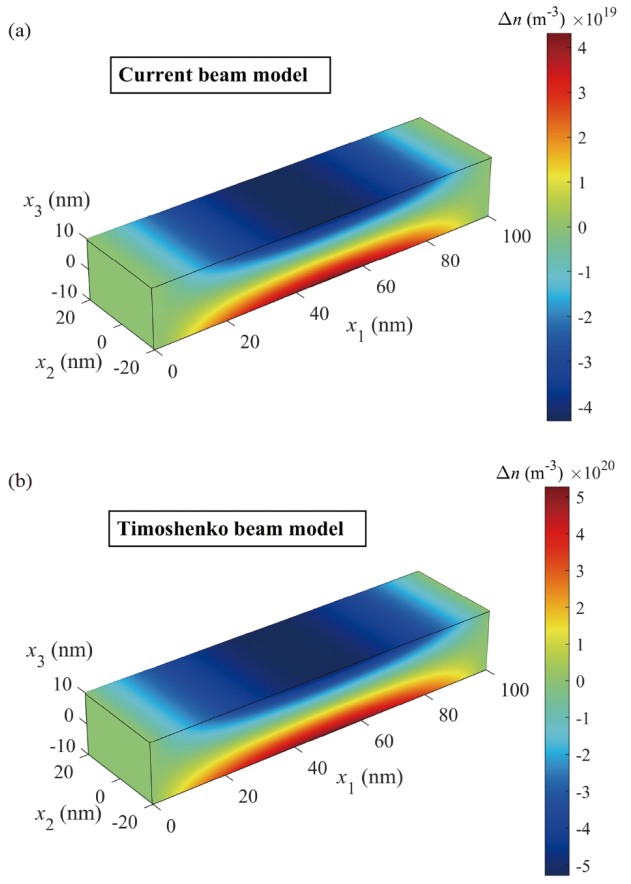

Figure 4 Effect of antisymmetric thickness-stretch on electron concentration perturbation: (a) current beam model and (b) Timoshenko beam model ($\ell = 1 \times 10^{-9}$ m, $n_0 = 1 \times 10^{21}$ m^{-3}, $\vartheta = 1$ N/m).

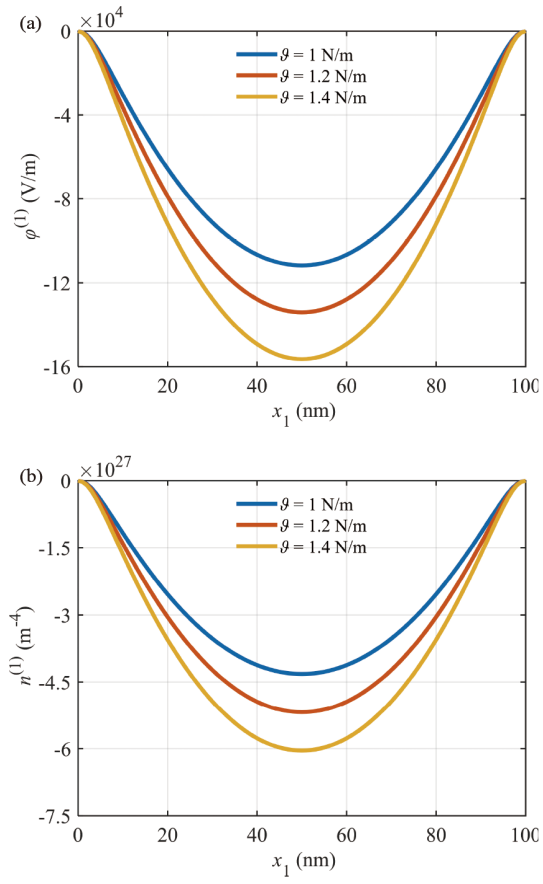

Figure 5 Effect of load magnitudes on (a) $\varphi^{(1)}$ and (b) $n^{(1)}$ ($\ell = 1 \times 10^{-9}$ m, $n_0 = 1 \times 10^{21}$ m^{-3}).

oelectronic properties within FS structures.

The magnitude of $\varphi^{(1)}$ and $n^{(1)}$ under varying ϑ and n_0 are explored as part of the parameter studies, as illustrated in Figs. 5 and 6. These figures reveal that increasing load magnitude significantly enhances both the electric potential and electron concentration. Particularly, the relationship between load magnitude and the related fields is linear at any specific point within the beam, as indicated by the linear differential equation (32). Figure 6(a) demonstrates that doping levels have a minor inhibitory influence on the electric potential. This behavior is attributed to the redistribution of electrons, which shield the flexoelectric polarization and result in a decrease in the electric potential's amplitude. The electric potential is expected to reach its peak when the semiconductor effect disappears. In contrast, when the value of n_0 is increased, the electromechanical interactions in the beam change more quickly. As a result, the electron concentration becomes highly responsive to changes in n_0, as shown in Fig. 6(b).

We extended our research to explore the tuning mechanism of microstructure and flexoelectric effects on mechanical displacements in the suggested beam model. Figure 7 (a)-(c) visualizes the variations of bending, fundamental thickness-shear, and antisymmetric thickness-stretch at the top surface of the beam along the axial direction x_1 with different length scale parameter ℓ, where the displacement curves neglecting both microstructure and flexoelectric effects are also plotted for comparison (depicted by the black solid line). Note that when the flexoelectric effect diminishes, the absence of the electric field hinders the interaction between mobile charges and displacements, thereby resulting in the disappearance of the semiconductor effect. Our observations bring to light that considering length scale parameters or flexoelectric coefficients will reduce all the displacements. This stiffening phenomenon can be attributed to the size-dependent effect at the micro and nanometer scales [13,56,57]. Furthermore, Fig. 7(a)-(c) illustrates that the microstructure effect significantly influences $u_3^{(0)}$, $u_1^{(1)}$, and $u_3^{(2)}$ of the beam, while the impact of the flexoelectricity is negligible for the specific material properties and geometry parameters examined in this study.

3.2 Wave propagation

In the second example study, we examine the propagation characteristics of straight-crested waves with infinite

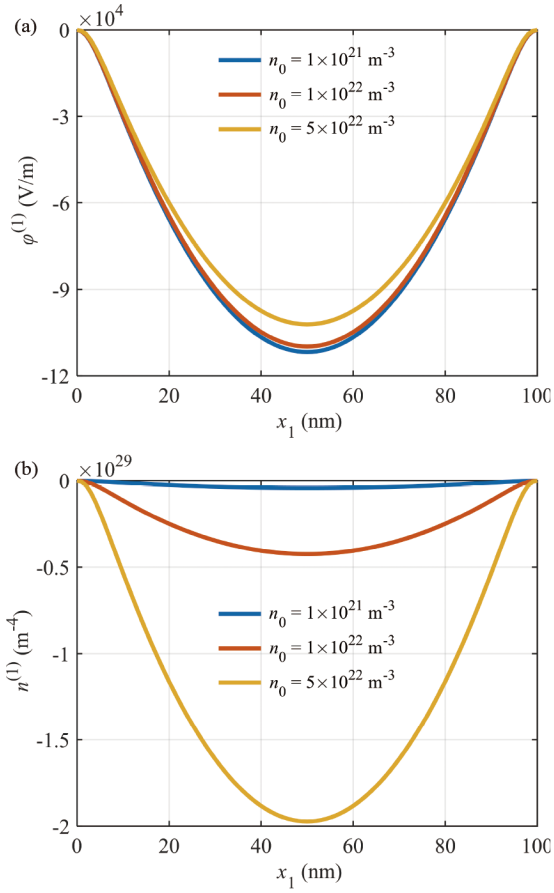

Figure 6 Effect of doping levels on (a) $\varphi^{(1)}$ and (b) $n^{(1)}$ ($\ell = 1 \times 10^{-9}$ m, $\vartheta = 1$ N/m).

boundaries ($L = \infty$) along the x_1 direction. Without body forces, the non-dimensional field variables in the beam can be assumed in the following form:

$$\begin{aligned}&\left\{U_3^{(0)}, U_3^{(2)}, \psi, N\right\} = \left\{\mathbb{W}^S, \mathbb{S}^S, \mathbb{Y}^S, \mathbb{N}^S\right\}\sin(\zeta X)\mathrm{e}^{\mathrm{i}\Omega\tau},\\ &U_1^{(1)} = \mathbb{V}^S\cos(\zeta X)\mathrm{e}^{\mathrm{i}\Omega\tau},\end{aligned} \tag{33}$$

where $\mathbb{W}^S$, $\mathbb{V}^S$, $\mathbb{S}^S$, $\mathbb{Y}^S$, and $\mathbb{N}^S$ are non-dimensional wave amplitudes, i is the imaginary unit satisfying $\mathrm{i}^2 = -1$, while ζ and Ω are denoted as the non-dimensional wave number and angular wave frequency, respectively.

Substituting Eq. (30) back into Eqs. (25a)-(25e) yields

$$\left\{[K_{ij}] + [M_{ij}]\right\}[\mathbb{W}^S, \mathbb{V}^S, \mathbb{S}^S, \mathbb{Y}^S, \mathbb{N}^S]^{\mathrm{T}} = 0, \tag{34}$$

where $[M_{ij}]$ is a 5 × 5 matrix detailed in Eq. (B2) in Appendix B.

For non-zero solutions, the determinant of the coefficient matrix in Eq. (34) must vanish. This determinant is stated as a power function that depends on the wave frequency and the wave number. In actual application, a numerical approach has been constructed to determine the dispersion relations. By supplying a sequence of wave numbers, the associated wave frequencies are determined to match the zero-determinant requirement. Consequently, this technique

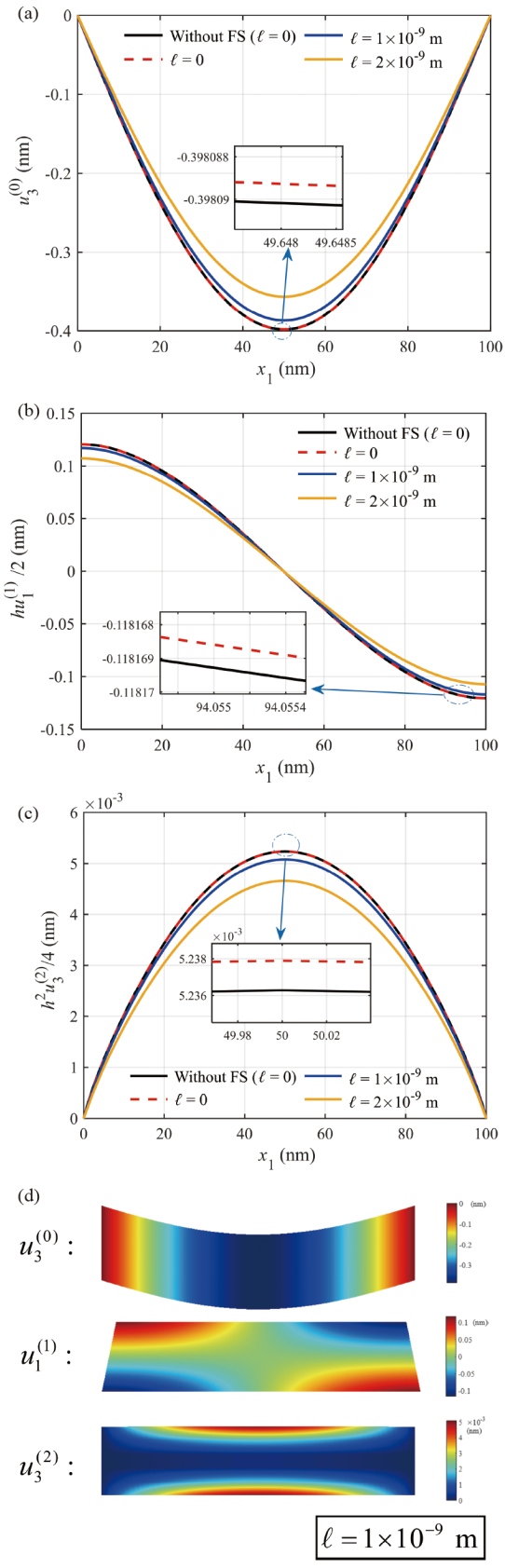

Figure 7 Variations of the mechanical displacements: (a) bending, (b) fundamental thickness-shear, (c) antisymmetric thickness-stretch, and (d) corresponding deformed shapes ($n_0 = 1 \times 10^{21}$ m^{-3}, $\vartheta = 1$ N/m).

permits the discovery of a total of nine dispersion relations. On the other hand, for any given combination of wave number and wave frequency satisfying a certain dispersion relation, the ratios among the five unknown wave amplitudes may be ascertained using Eq. (34).

Figure 8 displays the dispersion relations resulting from Eq. (34). The material parameters employed are consistent with those detailed in Sect. 3.1. Given the specified material and structure properties, only three groups of the nine dispersion relations demonstrate positive real wave frequencies, as electric waves are unable to propagate independently. In ascending sequence, they are designated as bending, fundamental thickness-shear, and antisymmetric thickness-stretch waves.

In Fig. 8, it becomes apparent that the wave frequency values corresponding to the antisymmetric thickness-stretch mode anticipated by the present model surpass those of the model lacking flexoelectric and semiconductor effects ("without FS"). Conversely, the frequencies associated with the other two waves remain consistent between the two models. To distinguish between the mechanisms of flexoelectric and semiconductor effects on the antisymmetric thickness-stretch waves, an analytical expression for the cutoff frequency of antisymmetric thickness-stretch in the proposed FS beam model is given by

$$W^{\mathrm{ATS}} = \frac{2\sqrt{15}\sqrt{\gamma + c_{11}(h^2 + 12\ell^2)}}{h^2\sqrt{\rho}}, \qquad \gamma = \frac{144\varphi_T f_{11}^2}{n_0 q h^2 + 12\varphi_T \varepsilon_{11}}, \tag{35}$$

where W^{ATS} is the cutoff frequency of antisymmetric thickness-stretch, and γ stands for the flexoelectric and semiconductor effects. Recall that the cutoff frequency here relates to the boundary frequency below which the waves cannot pass. From Eq. (35), it becomes evident that the incorporation of the flexoelectric effect (with $f_{11} \neq 0$) would always result in a higher W^{ATS}. Nevertheless, it is notable that W^{ATS} predicted by the current model diminishes as the semiconductor effect increases (i.e., as $n_0 \uparrow$). The comprehension of the wave motion mechanism is crucial for the optimization design of electroacoustic devices.

To further validate the accuracy of the results, the dispersion curves calculated based on linear elasticity theory (without flexoelectric and semiconductor effects) are compared with the exact solutions obtained using the multi-dimensional moduli ratio convergence method [58-60], as depicted in Fig. 9. It is evident that within the displayed range of wave numbers and wave frequencies, the approximate solution aligns closely with the exact one. Notably, the dispersion curves for bending waves in both cases are nearly identical, demonstrating the correctness of the theoretical model established in this study.

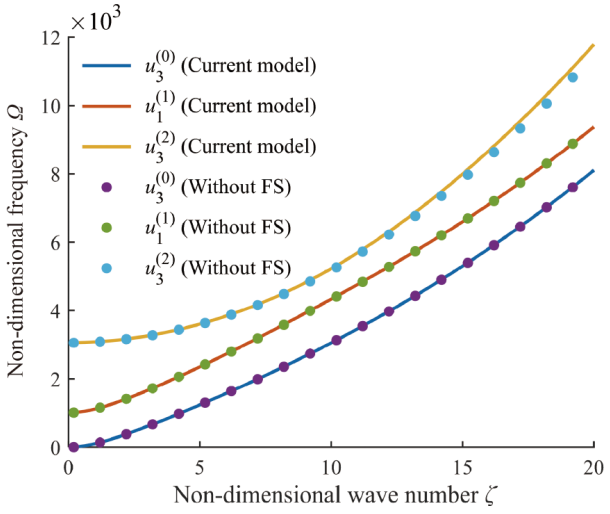

Figure 8 Dispersion relation of bending, fundamental thickness-shear, and antisymmetric thickness-stretch ($\ell = 1 \times 10^{-9}$ m, $n_0 = 1 \times 10^{21}$ m^{-3}, $b = 2h = 40$ nm).

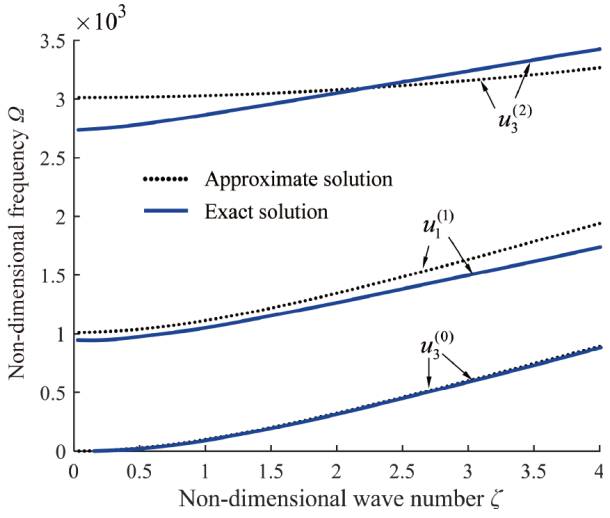

Figure 9 Dispersion relation of bending, fundamental thickness-shear, and antisymmetric thickness-stretch of the present approximate solution compared to the exact solution (without flexoelectric and semiconductor effects).

4. Concluding remarks

A new FS beam model integrating bending, fundamental thickness-shear, and antisymmetric thickness-stretch is established. The governing equations and complete BCs are developed through the PVW approach for FS, where microstructure, flexoelectric, and semiconductor effects are simultaneously treated in a cohesive framework. Numerical results in the static bending case underscore the critical significance of considering antisymmetric thickness-stretch in analyzing the flexoelectronic properties of nanobeams. The analytical investigation into wave propagation reveals that the wave frequencies of the antisymmetric thickness-stretch mode anticipated by the current model are higher

than those of the elastic model ignoring flexoelectric and semiconductor effects. Moreover, our analysis explores the intricate interplay between these effects on the cutoff frequency, elucidating their distinct contributions to wave motions.

Appendix A

For the FS beam exhibiting cubic symmetry (m3m point group), the elastic, dielectric, and carrier mobility and diffusion matrices are [25]

$$[\mathbf{c}]=\begin{bmatrix} c_{11} & c_{12} & c_{12} & 0 & 0 & 0 \\ c_{12} & c_{11} & c_{12} & 0 & 0 & 0 \\ c_{12} & c_{12} & c_{11} & 0 & 0 & 0 \\ 0 & 0 & 0 & c_{44} & 0 & 0 \\ 0 & 0 & 0 & 0 & c_{44} & 0 \\ 0 & 0 & 0 & 0 & 0 & c_{44} \end{bmatrix},$$
$$[\boldsymbol{\varepsilon}]=\begin{bmatrix} \varepsilon_{11} & 0 & 0 \\ 0 & \varepsilon_{11} & 0 \\ 0 & 0 & \varepsilon_{11} \end{bmatrix},\quad [\boldsymbol{\mu}^n]=\begin{bmatrix} \mu_{11}^n & 0 & 0 \\ 0 & \mu_{11}^n & 0 \\ 0 & 0 & \mu_{11}^n \end{bmatrix}, \tag{A1}$$
$$[\mathbf{D}^n]=\begin{bmatrix} D_{11}^n & 0 & 0 \\ 0 & D_{11}^n & 0 \\ 0 & 0 & D_{11}^n \end{bmatrix}.$$

For the sake of space, the flexoelectric coefficient can be written as [39,61]

$$\begin{aligned} &f_{1111}=f_{2222}=f_{3333}=f_{11}, \\ &f_{1133}=f_{2233}=f_{1122}=f_{2121}=f_{3232}=f_{3131}=f_{111}, \\ &f_{1221}=f_{1331}=f_{2112}=f_{2332}=f_{3223}=f_{3113}=f_{14}. \end{aligned} \tag{A2}$$

Appendix B

The non-zero components in the stiffness matrix $[K_{ij}]$ are detailed as follows:

$$\begin{aligned} &K_{11}=\mathbb{A}_2\xi_k^4-\mathbb{A}_1\xi_k^2,\ K_{12}=\mathbb{A}_4\xi_k^3-\mathbb{A}_3\xi_k, \\ &K_{13}=\mathbb{A}_6\xi_k^4-\mathbb{A}_5\xi_k^2,\ K_{14}=-\mathbb{A}_7\xi_k^2, \\ &K_{21}=\mathbb{B}_1\xi_k-\mathbb{B}_2\xi_k^3,\ K_{22}=\mathbb{B}_3-\mathbb{B}_4\xi_k^2+\mathbb{B}_5\xi_k^4, \\ &K_{23}=\mathbb{B}_6\xi_k-\mathbb{B}_7\xi_k^3,\quad K_{24}=\mathbb{B}_8\xi_k-\mathbb{B}_9\xi_k^3, \\ &K_{31}=\mathbb{C}_2\xi_k^4-\mathbb{C}_1\xi_k^2,\ K_{32}=\mathbb{C}_4\xi_k^3-\mathbb{C}_3\xi_k, \\ &K_{33}=\mathbb{C}_5-\mathbb{C}_6\xi_k^2+\mathbb{C}_7\xi_k^4,\ K_{34}=\mathbb{C}_8-\mathbb{C}_9\xi_k^2, \\ &K_{41}=-\mathbb{D}_1\xi_k^2,\ K_{42}=\mathbb{D}_3\xi^3-\mathbb{D}_2\xi_k, \\ &K_{43}=\mathbb{D}_4-\mathbb{D}_5\xi_k^2,\ K_{44}=\mathbb{D}_6-\mathbb{D}_7\xi_k^2, \\ &K_{45}=\mathbb{D}_8,\ K_{51}=\mathbb{E}_1-\mathbb{E}_2\xi_k^2,\ K_{52}=\mathbb{E}_3-\mathbb{E}_4\xi_k^2. \end{aligned} \tag{B1}$$

The non-zero components in the mass matrix $[M_{ij}]$ are detailed as follows:

$$\begin{aligned} &M_{11}=\Omega^2\mathbb{M}_1,\ M_{13}=\Omega^2\mathbb{M}_2,\ M_{22}=\Omega^2\mathbb{M}_3, \\ &M_{31}=\Omega^2\mathbb{M}_4,\ M_{33}=\Omega^2\mathbb{M}_5,\ M_{55}=-\mathrm{i}\Omega\mathbb{M}_6. \end{aligned} \tag{B2}$$

Conflict of interest *On behalf of all authors, the corresponding author states that there is no conflict of interest.*

Author contributions ***Ziwen Guo:*** *Investigation, Formal analysis, Methodology, Writing – Original draft.* ***Gongye Zhang:*** *Writing – Reviewing and Editing, Supervision.* ***Changwen Mi:*** *Writing – Reviewing and Editing, Supervision.*

Acknowledgements *This work was supported by the National Natural Science Foundation of China (Grant No. 12002086 (Gongye Zhang)), Fundamental Research Funds for the Central Universities (Grant No. 2242022R40040 (Gongye Zhang)), and Postgraduate Research & Practice Innovation Program of Jiangsu Province (Grant No. KYCX24_0365 (Ziwen Guo)).*

1 A. K. Tagantsev, V. Meunier, and P. Sharma, Novel electromechanical phenomena at the nanoscale: Phenomenological theory and atomistic modeling, MRS Bull. **34**, 643 (2009).
2 Q. Deng, S. Lv, Z. Li, K. Tan, X. Liang, and S. Shen, The impact of flexoelectricity on materials, devices, and physics, J. Appl. Phys. **128**, 080902 (2020).
3 L. Shu, R. Liang, Z. Rao, L. Fei, S. Ke, and Y. Wang, Flexoelectric materials and their related applications: A focused review, J. Adv. Ceram. **8**, 153 (2019).
4 Z. Guo, Y. Qu, G. Zhang, and C. Mi, Magnetically induced electromechanical fields in a flexoelectric composite microplate, Math. Mech. Solids **28**, 1091 (2023).
5 M. Lan, W. Yang, X. Liang, S. Hu, and S. Shen, Vibration modes of flexoelectric circular plate, Acta Mech. Sin. **38**, 422063 (2022).
6 G. Zhang, Y. Qu, Z. Guo, and F. Jin, Magnetically induced electric potential in first-order composite beams incorporating couple stress and its flexoelectric effects, Acta Mech. Sin. **37**, 1509 (2021).
7 J. Yang, Z. Chen, and Y. Hu, An exact analysis of a rectangular plate piezoelectric generator, IEEE Trans. Ultrason. Ferroelect. Freq. Contr. **54**, 190 (2007).
8 X. M. Yang, Y. T. Hu, and J. S. Yang, Electric field gradient effects in anti-plane problems of polarized ceramics, Int. J. Solids Struct. **41**, 6801 (2004).
9 Y. Zhao, X. Hou, S. Zhang, T. Sun, L. Du, and Z. Deng, Nonlinear forced vibration of thermo-electro-elastic piezoelectric-graphene composite nanoplate based on viscoelastic foundation, Acta Mech. Sin. **39**, 522228 (2023).
10 Y. Chen, Z. Yang, Z. Chen, K. Li, L. Wang, and S. Zhou, Theoretical and experimental investigations of multibifurcated piezoelectric energy harvesters with coupled bending and torsional vibrations, Acta Mech. Sin. **38**, 521434 (2022).
11 J. Narvaez, F. Vasquez-Sancho, and G. Catalan, Enhanced flexoelectric-like response in oxide semiconductors, Nature **538**, 219 (2016).
12 Z. Yan, and L. Jiang, Size-dependent bending and vibration behaviour of piezoelectric nanobeams due to flexoelectricity, J. Phys. D-Appl. Phys. **46**, 355502 (2013).
13 Y. L. Qu, Z. W. Guo, G. Y. Zhang, X. L. Gao, and F. Jin, A new model for circular cylindrical Kirchhoff-Love shells incorporating microstructure and flexoelectric effects, J. Appl. Mech. **89**, 121010 (2022).
14 K. Enakoutsa, A. D. Corte, and I. Giorgio, A model for elastic flexoelectric materials including strain gradient effects, Math. Mech. Solids **21**, 242 (2016).
15 A. R. El Dhaba, and M. E. Gabr, Flexoelectric effect induced in an

anisotropic bar with cubic symmetry under torsion, Math. Mech. Solids **25**, 820 (2020).
16 H. Ji, S. Shao, K. Liu, T. Wu, S. Shen, S. Zhang, and M. Xu, Giant flexoelectric response via mechanical and material design in elastomers, Mech. Mater. **165**, 104186 (2022).
17 L. Qi, S. Huang, G. Fu, A. Li, S. Zhou, and X. Jiang, Modeling of the flexoelectric annular microplate based on strain gradient elasticity theory, Mech. Adv. Mater. Struct. **26**, 1958 (2019).
18 A. Abdollahi, C. Peco, D. Millán, M. Arroyo, and I. Arias, Computational evaluation of the flexoelectric effect in dielectric solids, J. Appl. Phys. **116**, 093502 (2014).
19 Q. Deng, M. Kammoun, A. Erturk, and P. Sharma, Nanoscale flexoelectric energy harvesting, Int. J. Solids Struct. **51**, 3218 (2014).
20 M. C. Ray, Analysis of smart nanobeams integrated with a flexoelectric nano actuator layer, Smart Mater. Struct. **25**, 055011 (2016).
21 K. F. Wang, B. L. Wang, and S. Zeng, Analysis of an array of flexoelectric layered nanobeams for vibration energy harvesting, Compos. Struct. **187**, 48 (2018).
22 Z. Guo, Y. Qu, G. Zhang, and C. Mi, Second-order analysis of wave propagation in an MEE microbeam using Mindlin-Medick approximation, Acta Mech. **233**, 4141 (2022).
23 F. Liu, and H. Chu, An approach to calculate surface effects of polyhedron nanocrystals and its application in silicon nanowires, Acta Mech. Sin. **38**, 122097 (2022).
24 Z. Sun, T. Guo, K. I. Elkhodary, H. Yang, N. Zhou, and S. Tang, Localization and macroscopic instability in nanoporous metals, Acta Mech. Sin. **38**, 121538 (2022).
25 J. Yang, Analysis of Piezoelectric Semiconductor Structures (Springer, Cham, 2020).
26 Z. Guo, J. Chen, G. Zhang, C. Mi, and Y. Qu, Exact solutions for plane stress problems of piezoelectric semiconductors: Tuning free-carrier motions by various mechanical loadings, Eur. J. Mech.-A Solids **101**, 105073 (2023).
27 F. S. Hickernell, in The piezoelectric semiconductor and acoustoelectronic device development in the sixties: Proceedings of IEEE International Frequency Control Sympposium and PDA Exhibition Jointly with the 17th European Frequency and Time Forum, IEEE, Tampa, 2003, pp. 1012-1020.
28 Z. L. Wang, and J. Song, Piezoelectric nanogenerators based on zinc oxide nanowire arrays, Science **312**, 242 (2006).
29 Z. L. Wang, and W. Wu, Piezotronics and piezo-phototronics: fundamentals and applications, Natl. Sci. Rev. **1**, 62 (2014).
30 Z. L. Wang, W. Wu, and C. Falconi, Piezotronics and piezo-phototronics with third-generation semiconductors, MRS Bull. **43**, 922 (2018).
31 C. L. Zhang, Y. X. Luo, R. R. Cheng, and X. Y. Wang, Electromechanical fields in piezoelectric semiconductor nanofibers under an axial force, MRS Adv. **2**, 3421 (2017).
32 Y. Cao, Z. Guo, and Y. Qu, Static bending and forced vibration analyses of a piezoelectric semiconductor cylindrical shell within first-order shear deformation theory, Appl. Math. Model. **126**, 625 (2024).
33 Y. Cao, Z. Guo, and Y. Qu, Mechanically induced electric potential and charge redistribution in laminated composite piezoelectric semiconductor circular cylindrical thin shells, Thin-Walled Struct. **195**, 111372 (2024).
34 P. C. Lee, Y. L. Hsiao, J. Dutta, R. C. Wang, S. W. Tseng, and C. P. Liu, Development of porous ZnO thin films for enhancing piezoelectric nanogenerators and force sensors, Nano Energy **82**, 105702 (2021).
35 Y. Luo, R. Cheng, C. Zhang, W. Chen, and J. Yang, Electromechanical fields near a circular PN junction between two piezoelectric semiconductors, Acta Mech. Solid Sin. **31**, 127 (2018).
36 W. Yang, Y. Hu, and E. Pan, Tuning electronic energy band in a piezoelectric semiconductor rod via mechanical loading, Nano Energy **66**, 104147 (2019).
37 Y. Liang, W. Yang, and J. Yang, Transient bending vibration of a piezoelectric semiconductor nanofiber under a suddenly applied shear force, Acta Mech. Solid Sin. **32**, 688 (2019).
38 W. Yang, J. Liu, and Y. Hu, Mechanical tuning methodology on the barrier configuration near a piezoelectric PN interface and the regulation mechanism on I-V characteristics of the junction, Nano Energy **81**, 105581 (2021).
39 L. Wang, S. Liu, X. Feng, C. Zhang, L. Zhu, J. Zhai, Y. Qin, and Z. L. Wang, Flexoelectronics of centrosymmetric semiconductors, Nat. Nanotechnol. **15**, 661 (2020).
40 L. Sun, L. Zhu, C. Zhang, W. Chen, and Z. Wang, Mechanical manipulation of silicon-based Schottky diodes via flexoelectricity, Nano Energy **83**, 105855 (2021).
41 D. Guo, P. Guo, L. Ren, Y. Yao, W. Wang, M. Jia, Y. Wang, L. Wang, Z. L. Wang, and J. Zhai, Silicon flexoelectronic transistors, Sci. Adv. **9**, eadd3310 (2023).
42 M. H. Zhao, X. Liu, C. Y. Fan, C. Lu, and B. B. Wang, Theoretical analysis on the extension of a piezoelectric semi-conductor nanowire: Effects of flexoelectricity and strain gradient, J. Appl. Phys. **127**, 085707 (2020).
43 H. Li, L. Chu, Y. Li, G. Dui, and Q. Deng, Study on PN heterojunctions associated bending coupling in flexoelectric semiconductor composites considering the effects of size-dependent and symmetry-breaking, J. Appl. Phys. **132**, 125701 (2022).
44 Y. L. Qu, G. Y. Zhang, X. L. Gao, and F. Jin, A new model for thermally induced redistributions of free carriers in centrosymmetric flexoelectric semiconductor beams, Mech. Mater. **171**, 104328 (2022).
45 Y. Qu, F. Jin, and J. Yang, Effects of mechanical fields on mobile charges in a composite beam of flexoelectric dielectrics and semiconductors, J. Appl. Phys. **127**, 194502 (2020).
46 Y. Qu, F. Zhu, E. Pan, F. Jin, and H. Hirakata, Analysis of wave-particle drag effect in flexoelectric semiconductor plates via Mindlin method, Appl. Math. Model. **118**, 541 (2023).
47 G. Y. Zhang, Z. W. Guo, Y. L. Qu, and C. W. Mi, Global and local flexotronic effects induced by external magnetic fields in warping of a semiconducting composite fiber, Compos. Struct. **295**, 115711 (2022).
48 Y. Zheng, B. Huang, L. Yi, T. Ma, L. Xie, and J. Wang, Nonlinear thickness-shear vibration of an infinite piezoelectric plate with flexoelectricity based on the method of multiple scales, Appl. Math. Mech.-Engl. Ed. **43**, 653 (2022).
49 G. Zhang, and S. Shen, Analysis of electromechanical couplings and nonlinear carrier transport in flexoelectric semiconductors, J. Phys. D-Appl. Phys. **56**, 325102 (2023).
50 R. D. Mindlin, and J. Yang, An introduction to the mathematical theory of vibrations of elastic plates (World Scientific, Hackensack, 2006).
51 G. Wang, G. Nie, X. Liu, and J. Yang, Magnetically induced redistribution of mobile charges in bending of composite beams with piezoelectric semiconductor and piezomagnetic layers, Arch. Appl. Mech. **91**, 2949 (2021).
52 P. Germain, The method of virtual power in the mechanics of continuous media, I: Second-gradient theory, Math. Mech. Compl. Sys. **8**, 153 (2020).
53 R. D. Mindlin, and N. N. Eshel, On first strain-gradient theories in linear elasticity, Int. J. Solids Struct. **4**, 109 (1968).
54 B. S. Altan, and E. C. Aifantis, On some aspects in the special theory of gradient elasticity, J. Mech. Behav. Mater. **8**, 231 (1997).
55 S. M. Sze, and K. K. Ng, Physics of Semiconductor Devices (Wiley-Interscience, Hoboken, 2007).
56 U. K. Bhaskar, N. Banerjee, A. Abdollahi, Z. Wang, D. G. Schlom, G. Rijnders, and G. Catalan, A flexoelectric microelectromechanical system on silicon, Nat. Nanotech. **11**, 263 (2016).
57 H. M. Ma, X. L. Gao, and J. N. Reddy, A microstructure-dependent Timoshenko beam model based on a modified couple stress theory, J. Mech. Phys. Solids **56**, 3379 (2008).
58 J. Yang, The Mechanics of Piezoelectric Structures (World Scientific, New Jersey, 2006).
59 F. Zhu, B. Wang, and Z. Qian, A numerical algorithm to solve multivariate transcendental equation sets in complex domain and its

application in wave dispersion curve characterization, Acta Mech. **230**, 1303 (2019).
60 F. Zhu, N. Li, E. Pan, and Y. Qu, A new Stroh formalism for gradient electro-mechanics with applications to Lamb waves in piezoelectric and flexoelectric coupled plates, J. Appl. Phys. **135**, 114103 (2024).
61 L. Shu, X. Wei, T. Pang, X. Yao, and C. Wang, Symmetry of flexoelectric coefficients in crystalline medium, J. Appl. Phys. **110**, 104106 (2011).

考虑反对称厚度伸缩效应的挠曲电半导体纳米梁静态弯曲和波传播分析

郭子文, 章公也, 糜长稳

摘要 本文研究了在考虑弯曲、基本厚度剪切和反对称厚度伸缩变形情况下挠曲电半导体纳米梁中的机电耦合效应和电荷重分布问题. 所耦合的控制方程涵盖了微结构效应、挠曲电效应和半导体效应, 强调了机械位移、电势和载流子之间的相互耦合作用. 为便于挠曲电电子设备应用, 本文在所推导理论框架基础上解析求解了由均匀压力引起的挠曲电半导体简支梁的静态弯曲以及无限长挠曲电半导体梁的波传播问题. 特别是, 本文探讨了反对称厚度伸缩对机械位移和电子浓度扰动的影响, 揭示了微结构和挠曲电效应的尺寸依赖性. 研究发现, 与忽略挠曲电和半导体效应的模型相比, 反对称厚度伸缩波的频率更高, 本文首次从数学角度解释了这些效应对反对称厚度伸缩波截止频率的影响. 这些发现为提高挠曲电传感器和电声设备的性能提供了理论依据.